Congresso de Métodos Numéricos em Engenharia 2015
Lisboa, 29 de Junho a 2 de Julho 2015

DEBRIS FLOW MODELLING WITH HIGH-PERFORMANCE MESHLESS METHODS

Ricardo B. Canelas[1*], José M. Domínguez[2], Alexandro C. Crespo[2], Miguel Silva[3] and Rui M. L. Ferreira[1]

1: CEris
Instituto Superior Tcnico
University of Lisbon
Av. Rovisco Pais, Lisbon Portugal
e-mail: ricardo.b.canelas@ist.utl.pt, web: www.fluidmechenv.tk

2: EPHYSLAB
Universidade de Vigo
Ourense, Spain
e-mail: jmdominguez@uvigo.es web: www.ephyslab.uvigo.es

3: Aqualogus
Alameda dos Oceanos, Edifcio Mar do Oriente, Lote 1.07.1 AN 2.4, Parque das Naes, Lisbon
e-mail: msilva@aqualogus.pt web: www.aqualogus.pt/

Keywords: Instructions, Numerical Methods, Engineering, APMTAC, SEMNI, Lisboa

Abstract. *Debris flows represent some of the most relevant phenomena in geomorphological phenomena. Due to the potential destructiveness of such flows, they are the target of a vast amount of research. Numerical work traditionally focuses on unresolved single-phase solvers with modified rheological considerations, usually derived from simplified theoretical frameworks or experimental data. Due to the flow characteristics, both time and spatially resolved data are difficult to compile in an experimental set-up.*

The DualSPHysics meshless numerical implementation based on Smoothed Particle Hydrodynamics is expanded with a Distributed Contact Discrete Element Method in order to explicitly solve the fluid and the solid phase. This represents a resolved model, were no ad-hoc formulations are used concerning the momentum exchanges between the phases. The model is validated for buoyant flows and wet solid-solid interactions, using both analytical and experimental data. Implementation is done using optimized algorithms for massively parallel architectures.

An experimental set-up for stony debris flows in a slit check dam is reproduced numerically, with retention curves being derived and compared. The results show similar quantities of retained solid material, indicating that the model seems to provide reliable results and can provide both meaningful industry solutions and new research prompts regarding debris flows.

1 INTRODUCTION

Debris flows are regarded as one of the most feared flow-related phenomena, due to the large destructive potential of infrastructure and danger to human lives. It is no surprise that a large body of work has been produced concerning its genesis, behavior and mitigation measures, both by fundamental phenomenological approaches reduced to analytic or simplified numerical problems and experimental campaigns. The flow characteristics ensure that complex measurements on important quantities remain difficult to perform. The inwards of a debris flow has only been accessible by analogy with simpler flows and conceptual work. Hope is therefore deposited in numerical work, to provide increasingly plausible insights into the mechanics of the flow. The amount of data amassed does not meet a reliable numerical solution, however. Existing conceptual models map poorly to a satisfactory numerical solution: the span of spacial scales involved in these flows start at the smaller energy carrying flow structures, up to the largest particles in the flow, possibly in the order of meters; the time scales range from millisecond inter-particle collisions to the duration of the flow; large deformations on the non-continuous multiphasic medium difficult any traditional approximation and the highly unsteady flow and free-surface deformations pose a challenge for state-of-the-art Finite-Volume codes, considering just single phase flows.

This work presents a relatively new approach to model these phenomena, using meshless methods. Recent advances in computer architectures, namely the introduction of massively parallel resources for consumer machines paved the way to explore these more computationally intensive methods. DualSPHysics [7] is a high performance meshless numerical implementation, based on Smoothed Particle Hydrodynamics (SPH). The model has been extensively validated for fluid flows [6, 1, 2], gracefully dealing with complex, time evolving geometries and unsteady free surface conditions. Introducing solid bodies with no kinematic restrictions leaded to successful buoyancy tests [5]. Further expanding the model with a Distributed Contact Discrete Element Method (DCDEM) [4], fully arbitrary fluid-solid interactions are introduced, with a relatively small set of conceptual assumptions. This represents a resolved model, were no ad-hoc formulations are used concerning the momentum exchanges between the phases, bypassing the need for a simplified conceptual model for specific scenarios, such as debris flow.

The application of the model to a debris flow is done by reproducing an experimental campaign where debris flow mitigation measures are studied. This experimental activity was part of the *R&D* project STOPDEBRIS, which was funded by QREN and developed by a multidisciplinary team from AQUALOGUS, Engenharia e Ambiente, in partnership with CEris-IST. A flume is fitted with a check-dam, intended to control the transport and deposition processes of the sediments carried downstream by debris flows. Since check-dams are considered as one of the simplest and most effective engineering measures against debris flows [19, 16] they were widely applied all over the world as a short-term mitigation measure. Check dams are composed of a weir, two wings and a robust foundation,

although there are a variety of other check dam solutions. Open-type check dams present a very attractive characteristic: they allow small sediment particles to pass through, while trapping larger blocks. The implemented open-type check dam is a slit dam, whose effectiveness in debris flows mitigation has been documented in the literature.

The objective of this paper is to introduce and discuss the preliminary results of the SPH-DCDEM model by comparing with an experimental study. This should provide a good indication on the qualities of the model concerning the macro-scale results of a fully resolved debris flow.

2 FORMULATION

In SPH, the fluid domain is represented by a set of nodal points where physical properties such as mass, velocity, pressure and vorticity are known. These points move with the fluid in a Lagrangian manner and their properties change with time due to the interactions with neighbouring particles. The therm Smoothed Particle Hydrodynamics arises from the fact that the nodes, for all intended means, carry the mass of a portion of the medium, hence being easily labelled as Particles, and their individual angular velocity is disregarded, hence the Smooth. The method relies heavily on integral interpolant theory [14], that can be resumed to the exactness of

$$A\left(\boldsymbol{r}\right)=\int_{\Omega}A\left(\boldsymbol{r}'\right)\ \delta\left(\boldsymbol{r}-\boldsymbol{r}'\right)d\boldsymbol{r}', \tag{1}$$

for any continuous function $A(\boldsymbol{r})$ defined in $\boldsymbol{r}'$, where δ is the Dirac delta function and r is a distance. The nature of the Dirac delta function renders this identity useless however, and an approximation at $\boldsymbol{r}$ can be obtained by replacing it with a suitable weight function W, called a kernel function. W should be an even function, defined on a compact support, *i.e.* if the radius is ϵh then $W(\boldsymbol{r}-\boldsymbol{r}',h)=0$ if $|\boldsymbol{r}-\boldsymbol{r}'|\geq\epsilon h$, with $\lim_{h\to0}W=\delta$ and $\int_{\Omega}W\left(\boldsymbol{r}',h\right)d\boldsymbol{r}'=1$, where h is the smoothing length and defines the size of the kernel support. This leads to

$$A\left(\boldsymbol{r}\right)=\int_{\Omega'}A\left(\boldsymbol{r}'\right)\ W\left(\boldsymbol{r}-\boldsymbol{r}',h\right)d\boldsymbol{r}', \tag{2}$$

known as the integral interpolant. An approximation to discrete Lagrangian points can be made, by a proper discretization of the kernel function

$$A_i\approx\sum_j A_jV_jW(\boldsymbol{r}_{ij},h), \tag{3}$$

called the summation interpolant, extended to all particles j, $|\boldsymbol{r}_{ij}|=|\boldsymbol{r}_i-\boldsymbol{r}_j|\leq\epsilon h$, where V_j is the volume of particle j and A_i is the approximated variable at particle i. The cost of such approximation is that particle first order consistency, i.e., the ability of the kernel

approximation to reproduce exactly a first order polynomial function, may not be assured by the summation interpolant, since

$$\sum_j V_j W(\boldsymbol{r}_{ij}, h) \approx 1, \tag{4}$$

which is speciality understandable in situations were the kernel function does not verify compact support, for example near the free surface or other open boundaries. Forcing the summation to equal 1 is called the *Shepard* correction

$$A_i = \frac{\sum_j A_j V_j W(\boldsymbol{r}_{ij}, h)}{\sum_j V_j W(\boldsymbol{r}_{ij}, h)}, \tag{5}$$

restoring up to 1^{st} order consistency, for non-uniform distributions and incomplete support. A spacial first order derivative can be written as

$$\begin{aligned} \boldsymbol{\nabla} \boldsymbol{A}\left(\boldsymbol{r}\right) = \int_{\Omega'} \boldsymbol{\nabla}_{\boldsymbol{r}'} \boldsymbol{A}\left(\boldsymbol{r}'\right)\ W\left(\boldsymbol{r}-\boldsymbol{r}'\right) d\boldsymbol{r}' \Rightarrow \\ \boldsymbol{\nabla} \boldsymbol{A}_i \approx \sum_j \boldsymbol{A}_j V_j \boldsymbol{\nabla} W(\boldsymbol{r}_{ij}, h), \end{aligned} \tag{6}$$

but it is also subject to corrections in order to ensure consistency up to the desired precision [14].

3 DISCRETIZATION OF GOVERNING EQUATIONS

3.1 Equations of Motion in SPH

The nature of the classical SPH formulation renders an incompressible system difficult to model [9], and as a result most studies rely on the discretization of the compressible Navier-Stokes system

$$\frac{d\boldsymbol{v}}{dt} = -\frac{\boldsymbol{\nabla} p}{\rho} + \boldsymbol{\nabla} \boldsymbol{\tau} + \boldsymbol{g} \tag{7}$$

$$\frac{d\rho}{dt} = -\rho \boldsymbol{\nabla} \boldsymbol{v}, \tag{8}$$

where $\boldsymbol{v}$ is the velocity field, p is the pressure, ρ is the density and τ and g are the stress tensor and body forces, respectively. The continuity equation is traditionaly discretized by employing the notion that $\rho \boldsymbol{\nabla} \boldsymbol{v} = \boldsymbol{\nabla}(\rho \boldsymbol{v}) - \boldsymbol{v} \boldsymbol{\nabla} \rho$, rendering equation (8)

$$\frac{d\rho_i}{dt} = -\rho_i \sum_j m_j (\boldsymbol{v}_i - \boldsymbol{v}_j) \boldsymbol{\nabla} W(\boldsymbol{r}_{ij}, h) \tag{9}$$

This produces a zero divergence field for a $\boldsymbol{v} = k$ field. Equation (7) can be written as

$$\begin{aligned}\frac{d\boldsymbol{v}_i}{dt} = &-\sum_j m_j \left(\frac{p_i}{\rho_i^2} + \frac{p_j}{\rho_j^2}\right) \boldsymbol{\nabla} W(\boldsymbol{r}_{ij}, h) + \\ &+\sum_j m_j \left(\frac{4\mu \boldsymbol{r_{ij}} \boldsymbol{\nabla} W(\boldsymbol{r}_{ij}, h)}{(\rho_i + \rho_j)(|r_{ij}|^2 + \eta^2)}\right) \boldsymbol{v}_{ij} + \\ &+\sum_j m_j \left(\frac{\tau_i}{\rho_i^2} + \frac{\tau_j}{\rho_j^2}\right) \boldsymbol{\nabla} W(\boldsymbol{r}_{ij}, h) + \boldsymbol{g}\end{aligned} \tag{10}$$

The first term of the right side is a symmetrical, balanced form of the pressure term [14]. The second and third terms represent a laminar viscosity term [15] and a sub-partcile stress (SPS) [8], respectivley. The SPS term introduces the effects of turbulent motion at smaller scales than the spatial discretization. Following the eddy viscosity assumption and using Favre-averaging, the SPS stress tensor for a compressible fluid can be written as

$$\frac{\boldsymbol{\tau}_{\alpha\beta}}{\rho} = 2\nu_t \left(\boldsymbol{S}_{\alpha\beta} - \frac{1}{3}\boldsymbol{\delta}_{\alpha\beta}\boldsymbol{S}_{\alpha\beta}\right) - \frac{2}{3} C_I \Delta^2 \boldsymbol{\delta}_{\alpha\beta} |\boldsymbol{S}_{\alpha\beta}|^2, \tag{11}$$

where $\tau_{\alpha\beta}$ is the sub-particle stress tensor, $\nu_t = (C_S|\boldsymbol{r}_{ij}|)^2|\boldsymbol{S}_{\alpha\beta}|$ is the eddy viscosity, C_S is the Smagorinsky constant, $C_I = 6.6 \times 10^{-3}$ and $\boldsymbol{S}_{\alpha\beta}$ is the local strain rate tensor, with $|\boldsymbol{S}_{\alpha\beta}| = (2\boldsymbol{S}_{\alpha\beta}\boldsymbol{S}_{\alpha\beta})^{1/2}$.

Newton's equations for rigid body dynamics are discretized as

$$M_I \frac{d\boldsymbol{V}_I}{dt} = \sum_{k \in I} m_k \boldsymbol{f}_k \tag{12}$$

$$I_I \frac{d\boldsymbol{\Omega}_I}{dt} = \sum_{k \in I} m_k (\boldsymbol{r}_k - \boldsymbol{R}_I) \times \boldsymbol{f}_k, \tag{13}$$

where body I possesses a mass M_I, velocity $\boldsymbol{V}_I$, inertial tensor $\boldsymbol{I}_I$, angular velocity $\boldsymbol{\Omega}_I$ and center of gravity $\boldsymbol{R}_I$. $\boldsymbol{f}_k$ is the force by unit mass applied to particle k, belonging to body I. This force encompasses body forces, fluid resultants as well as the result of any rigid contact that might occur.

3.2 Rigid contact considerations for DEM particles

The contact force $\boldsymbol{F}_i^T$ acting on particle i resulting from collision with particle j is decomposed into $\boldsymbol{F}_n$ and $\boldsymbol{F}_t$, normal and tangential components respectively. Both of these forces are further decomposed into a repulsion force, $\boldsymbol{F}^r$, that takes into account the deformation of the particle, and a damping force, $\boldsymbol{F}^d$, for the dissipation of energy during the deformation.

In the current work, the normal forces are given by a modified, non-linear, Hertzian model [12]

$$\boldsymbol{F}_{n,ij} = \boldsymbol{F}_n^r + \boldsymbol{F}_n^d = k_{n,ij}\delta_{ij}^{3/4}\boldsymbol{e}_{ij} - \gamma_{n,ij}\delta_{ij}^{1/4}\dot{\delta}_{ij}\boldsymbol{e}_{ij}, \tag{14}$$

where $k_{n,ij}$ is the stiffness constant of pair ij, $\delta_{ij} = \max(0, (d_i + d_j)/2 - |\boldsymbol{r_{ij}}|)$ is the particle overlap, $\boldsymbol{e}_{ij}$ is the unit vector between the two mass centres and $\gamma_{n,ij}$ is the damping constant. The stiffness and damping constants are given by [12]

$$k_{n,ij} = \frac{4}{3}E^*\sqrt{R^*}; \quad \gamma_{n,ij} = C_n\sqrt{6M^*E^*\sqrt{R^*}}, \tag{15}$$

with C_n of the order of 10^-5. The other parameters are given by

$$\frac{1}{E^*} = \frac{1-\nu_I^2}{E_I} + \frac{1-\nu_J^2}{E_J}; \quad R^* = \frac{r_i r_j}{r_i + r_j}; \quad M^* = \frac{m_I m_J}{m_I + m_J}, \tag{16}$$

where E is the Young modulus, ν is the Poisson ratio and m is the mass of the body.

Regarding tangential contacts, the complex mechanism of friction is modelled by a linear dash-pot bounded above by the Coulomb friction law. The Coulomb law is modified with a sigmoidal function in order to make it continuous around the origin regarding the tangential velocity [18]. One can write

$$\boldsymbol{F}_{t,ij} = \min(\mu_{IJ}\boldsymbol{F}_{n,ij}\tanh(8\dot{\delta}_{ij}^t)\boldsymbol{e}_{ij}^t; \quad \boldsymbol{f}_t^r + \boldsymbol{f}_t^d), \tag{17}$$

where

$$\boldsymbol{F}_t^r + \boldsymbol{F}_t^d = k_{t,ij}\delta_{ij}^t\boldsymbol{e}_{ij}^t - \gamma_{t,ij}\dot{\delta}_{ij}^t\boldsymbol{e}_{ij}^t \tag{18}$$

μ_{IJ}, the friction coefficient at the contact of I and J, should be expressed as a function of the two friction coefficients of the distinct materials. The stiffness and damping constants are derived to be $k_{t,ij} = 2/7k_{n,ij}$ and $\gamma_{t,ij} = 2/7\gamma_{n,ij}$ [10], as to insure internal consistency of the time scales required for stability. This mechanism models the static and dynamic friction mechanisms by a penalty method. The body does not statically stick at the point of contact, but is constrained by the spring-damper system.

3.3 Pressure Field Recovery, Stability Region and Particle Movement

The presented compressible formulation of SPH for the Navier-Stokes employs an equation of state to determine the pressure field, in order not to solve an additional partial differential equation, that relies on the correct tracking of a free surface, such as the Poisson equation [11]. Following [14], the commonly used estimate relationship between pressure and density is Tait's equation

$$p_i = \frac{\rho_0 c_0^2}{\gamma}\left[\left(\frac{\rho_i}{\rho_0}\right)^\gamma - 1\right] \tag{19}$$

where ρ_0 is a reference density, c_0 is a numerical sound celerity and $\gamma = 7$ for a fluid like water. According to equation 19, the compressibility of the fluid depends on c_0, in such a way that for a hight enough sound celerity the fluid is virtually incompressible. However the value of c_0 in the model should not be the actual speed of sound since this value is present in the definition of the stability region of the scheme. The stability region must be modified to accommodate another restriction, the DEM compatible time-step. The *CFL* condition can be written as

$$\Delta t = C \min\left[\min_i\left(\sqrt{\frac{h}{|\boldsymbol{f}_i|}}\right);\quad \min_i\left(\frac{h}{c_0 + \max_j|\frac{h\boldsymbol{v}_{ij}\boldsymbol{r}_{ij}}{\boldsymbol{r}_{ij}^2}|}\right);\quad \min_i\left(\pi/C50\sqrt{\frac{k_{n,ij}}{M^*}}\right)\right], \tag{20}$$

where C is the *CFL* constant of the order of 10^{-1} determined in accordance with the case. The first term results from the consideration of force magnitudes, the second is a combination of the *CFL* condition for numerical information celerities and a restriction arising from the viscous terms [9] and the third term takes into account a theoretical solution for the DEM stability constraints, that disregards the *CFL*. If the sound celerity in the simulation is too high, it will render Δt very small and the computation more expensive. Following [14], c_0 is kept to an artificial value of around 10 times the maximum flow speed, restricting the relative density fluctuations at less than 1%. As a consequence, the estimated pressure field by equation (19) usually shows some instabilities and may be subject to scattered distributions. The diffusive terms introduced in [13], designed to smooth the oscillations in the pressure field are used in equation (8). These terms do not allow a hydrostatic solution since a net force is developed near the free surface, but the test cases in this work represent a very unsteady flow, for which such terms are acceptable. Come complex formulations incur on much more expensive computations [3].

4 MODEL SET-UP

The simulations are based on a flume described in [17], where vertical slits with a spacing s, a 20% slope and a recirculating mechanism are the main characteristics. The numerical flume presents fully periodic conditions, allowing for both fluid and solid phase recirculation. Two slit typologies were tested, named P1 and P2, as defined in [17]. Three spacings were tested, $s/d95 \in [1.18; 1.36; 1.49]$, as per the experiments.

The scales of the sediment grain interactions are orders of magnitude inferior to the d50 of the granulometric curve. This may represent a problem for the numerical discretization, as even smaller distances need to be evaluated for the force computations (Equation 14), and machine precision can start to affect the computations after a large number of iterations. In order to curb such effect, the geometric scale of the numerical experiment was doubled, as

$$\lambda_l = \frac{L_m}{L_p} = 2 \tag{21}$$

where λ_l is the geometrical scale, L_m is the characteristic length of the model and L_p the same length on the physical prototype. Assuming Froude similarity, the discharges scale as

$$\lambda_Q = \frac{\lambda_V}{\lambda_t} = \frac{\lambda_l^3}{\lambda_l^{1/2}} = \lambda_l^{5/2} \tag{22}$$

It is considered that liquid and solid discharges introduced upstream are independent, i.e., it is not intended that the solid discharge corresponds to the capacity discharge for the given liquid discharge, considering the inclination, geometry and roughness of the flume. Table 1 shows the used model discharges and the corresponding prototype values.

	Prototype	Model
$Q_l(m^3s^{-1})$	0.018	0.1018
$Q_s(m^3s^{-1})$	0.00033	0.0018

Table 1: Model and prototype discharges

To promote a correct inlet of solid material, a hopper is modelled, placed on top of the channel. It was heuristically dimensioned to ensure an average solid discharge compatible with the one presented in Table 1. Solid sediment grain sizes are generated according to a random algorithm that reproduces a log-normal function, effectively approximating the granulometric curve from [17]. The grains are dispersed in the hopper and are let to achieve their natural equilibrium positions at the start of the simulation. The proposed initial conditions generator allows to generate two entirely distinct solutions based on the same granulometric curves, corresponding to several experimental runs.

The proposed parameters for the material properties, used in Equations 14 to 18, are summarised in Table 2.

$E(GNm^{-2})$	45
$\nu(-)$	0.35
$\mu(-)$	0.35

Table 2: Sediment mechanical characteristics

The resolution of the model was set at 0.008 m, resulting in over 1.6×10^6 particles. An overview of the domain can be seen in Figure 1.

5 PRELIMINARY RESULTS

The sediment trapping efficiency is accounted by measuring the solid discharges at a position sufficiently upstream and immediately downstream of the dam. The experimental

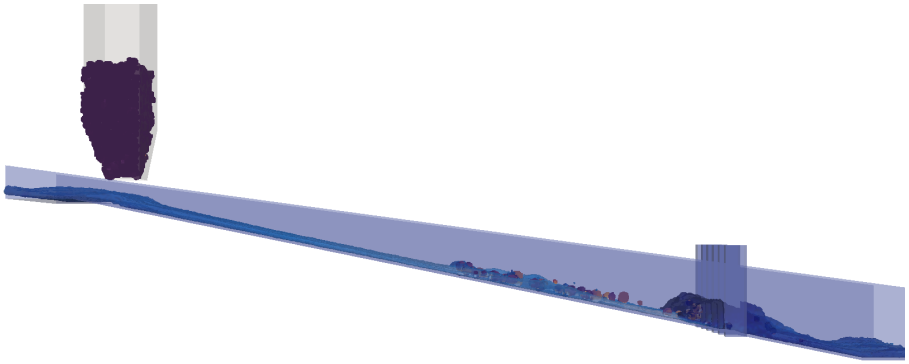

Figure 1: Overall domain configuration.

procedure applied volumes, but due to the recirculation of solid particles, for the analysis of the numerical solution such approach is impractical.

Immediately after the opening of the hopper, a substantial amount of material falls to the flume, as indicated in Figure 2, at $t = 3.0\ s$.

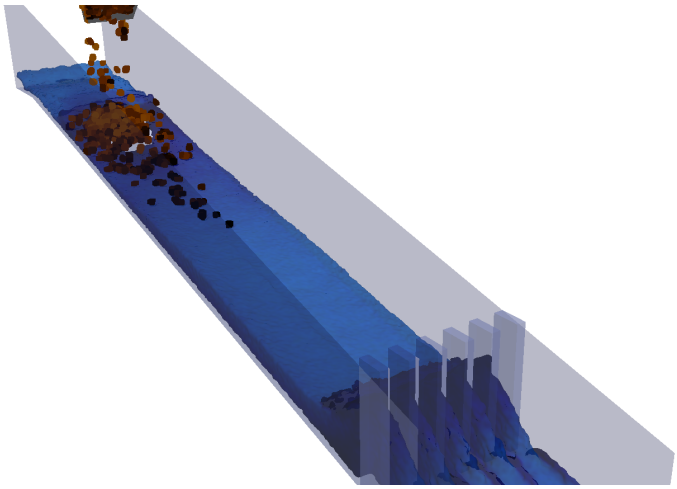

Figure 2: P1 type slits, $t = 3.0\ s$

As the material is carried downstream, deposition starts at the dam section. Figure 3 shows in detail a render of the solution in the dam area, at $t = 8.0\ s$.

As the material is dispensed from the hopper, the retention upstream of the dam becomes more effective. At $t = 35.0\ s$, the state of the solution is represented in Figure 4.

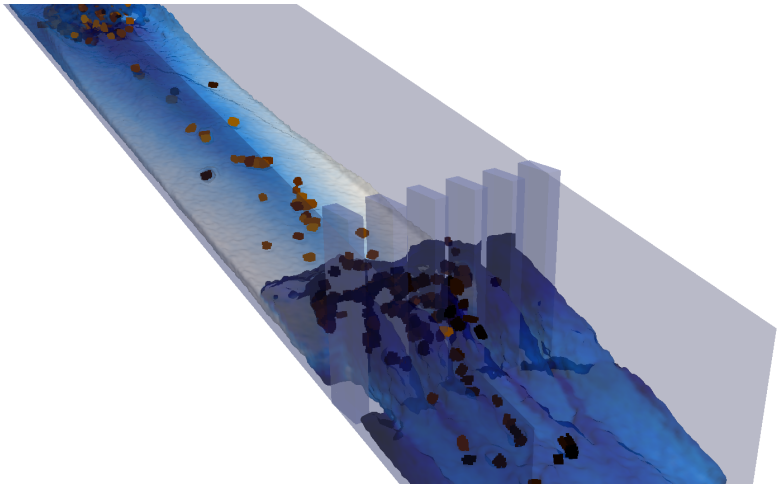

Figure 3: P1 type slits, $t = 8.0\ s$

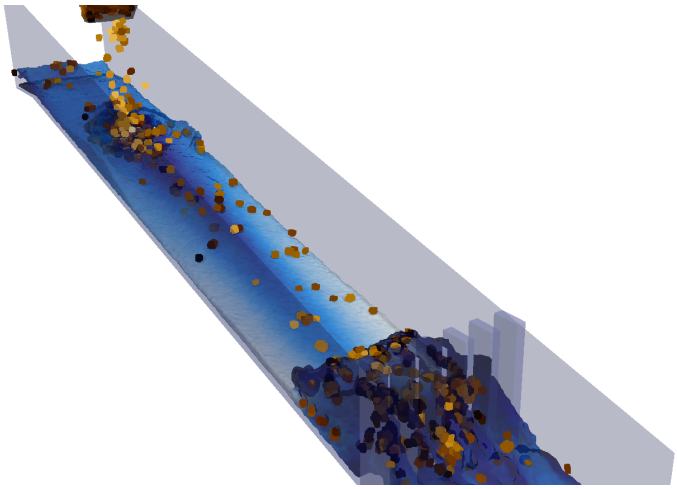

Figure 4: P1 type slits, $t = 35.0\ s$

Figures 2 to 4 are rendered from a particular simulation. As the sediment particles are generated with a random arrangement as initial conditions, significant instantaneous variations occur if one compares similar runs. On average, at $t = 40.0\ s$ the hopper is exhausted and the flow is assumed to reach equilibrium conditions close to 10 s after that, when the last solid particle reaches the backwater of the dam. A 15 s interval was used to count solid discharges and derive retention trapping rates. Figures 5 and 6 show the relationship between sediment trapping efficiency, E, and the relative spacing $s/d95$ for each tested solution.

The numerical results present a good comparison with the experimental data. A noticeable under prediction of the efficiency for small spacings is shown, for both slit geometries.

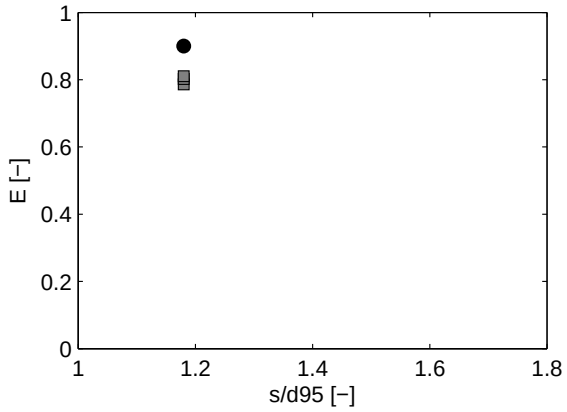

Figure 5: Sediment trapping efficiency results. P1 type slits. Experimental (·) Numerical (□)

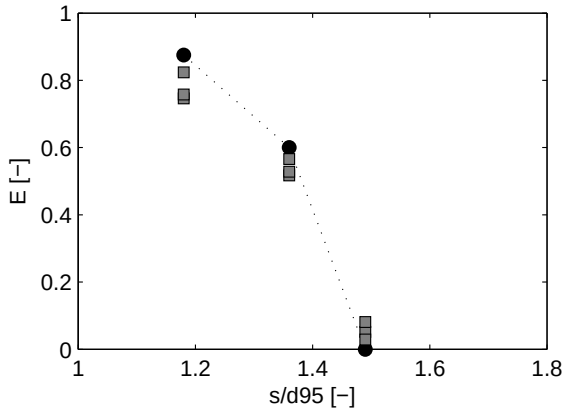

Figure 6: Sediment trapping efficiency results. P2 type slits. Experimental (·) Numerical (□)

For P2 slits the trend is accompanied with increasing spacing, but no zero efficiency is established for $s/d95 = 1.49$, contrasting with the experimental results. This is due to single sediment particles getting retained for long enough to affect the measurements.

The differences should be explained both by discretization shortcomings and differences in the initial conditions from the experimental to numerical experiments. Besides conceptual considerations, the doubling of the geometrical dimensions to allow for more relaxed length and time scales is bound to introduce differences in the flow depth in the locus of the dam. This is because Froude similarity is not an exact hypothesis in the vicinity of the slits. This may affect the retention properties of the numerical dam, but insufficient experimental data is available to provide more insight. Another important difference is related to the experimental procedure initial conditions, that are not marked by a smooth, fixed bed: an approximately 5 cm thick layer of sediment is deposited along the flume, also contributing to the total amount of mobile solid material if the flow is

capable of mobilizing it, besides introducing considerable resistance to the flow.

6 CONCLUSIONS

The work details a high-performance meshless method, capable of dealing with arbitrarily defined fluid-solid flows. An experimental campaign concerning stony debris flows is reproduced, with comparable results being drawn, despite significant differences in the conditions of the tests. The data points present maximum deviations of 9% to the experimental data, well within the variation of experimental runs of the same test. The model provides relevant data, that can greatly enrich experimental efforts. Further work on initial conditions and performance aspects is on course, hopefully improving both the approximation of the experimental runs and the overall performance of the DualSPHysics model.

ACKNOWLEDGEMENTS

This research was partially supported by project PTDC/ECM/117660/2010, funded by the Portuguese Foundation for Science and Technology (FCT). First author acknowledges FCT for his PhD grant, SFRH/BD/75478/2010. It was also partially funded by Xunta de Galicia under project Programa de Consolidacin e Estructuracin de Unidades de Investigacin Competitivas (Grupos de Referencia Competitiva), financed by European Regional Development Fund (FEDER) and by Ministerio de Economa y Competitividad under de Project BIA2012-38676-C03-03.

REFERENCES

[1] Altomare, C., A. Crespo, B. Rogers, J. Domínguez, G. X., and M. Gómez-Gesteira (2014). Numerical modelling of armour block sea breakwater with smoothed particle hydrodynamics. *Computers and Structures 130*, 34–45.

[2] Altomare, C., A. J. Crespo, J. M. Domnguez, M. Gmez-Gesteira, T. Suzuki, and T. Verwaest (2015). Applicability of smoothed particle hydrodynamics for estimation of sea wave impact on coastal structures. *Coastal Engineering 96*(0), 1 – 12.

[3] Antuono, M., A. Colagrossi, and S. Marrone (2012). Numerical diffusive terms in weakly-compressible sph schemes. *Computer Physics Communications 189*.

[4] Canelas, R., A. Crespo, J. Domínguez, and R. Ferreira (2013). A generalized sph-dem discretization for the modelling of complex multiphasic free surface flows. In 8^{th} *international SPHERIC workshop*.

[5] Canelas, R., J. Domínguez, A. Crespo, M. Góimez-Gesteira, and R. Ferreira (2015). A smooth particle hydrodynamics discretization for the modelling of free surface flows and rigid body dynamics. *International Journal for Numerical Methods in Fluids* (in press).

[6] Crespo, A., J. Domínguez, B. A., M. Gómez-Gesteira, and R. B.D. (2011). GPUs, a new tool of acceleration in CFD: Efficiency and reliability on smoothed particle hydrodynamics methods. *PLoS ONE 6(6)*.

[7] Crespo, A., J. Domínguez, B. Rogers, M. Gómez-Gesteira, S. Longshaw, R. Canelas, R. Vacondio, A. Barreiro, and O. García-Feal (2015). Dualsphysics: open-source parallel cfd solver on smoothed particle hydrodynamics (sph). *Computer Physics Communications 187*, 204–216.

[8] Dalrymple, R. and B. Rogers (2006). Numerical modeling of water waves with the sph method. *Coastal Engineering 53*(2-3), 141 – 147. Coastal Hydrodynamics and Morphodynamics.

[9] Gómez-Gesteira, M., B. Rogers, A. Dalrymple, R., and A. Crespo (2010). State-of-the-art of classical sph for free-surface flows. *Journal of Hydraulic Research 48*, 6–27.

[10] Hoomans, B. (2000, January). *Granular dynamics of gas-solid two-phase flows*. Ph. D. thesis, University of Twente, Enschede.

[11] Lee, E., D. Violeau, R. Issa, and S. Ploix (2010). Application of weakly compressible and truly incompressible sph to 3d water collapse in waterworks. *Journal of Hydraulic Research 48*.

[12] Lemieux, M., G. Lonard, J. Doucet, L. Leclaire, F. Viens, J. Chaouki, and F. Bertrand (2008). Large-scale numerical investigation of solids mixing in a v-blender using the discrete element method. *Powder Technology 181*(2), 205 – 216.

[13] Molteni, D. and A. Colagrossi (2009). A simple procedure to improve the pressure evaluation in hydrodynamic context using the sph. *Comput. Phys. Comm 180*, 861–872.

[14] Monaghan, J. (2005). Smoothed particle hydrodynamics. *Reports on Progress in Physics 68*(8), 1703.

[15] Morris, J. P., P. J. Fox, and Y. Zhu (1997). Modeling low reynolds number incompressible flows using sph. *Journal of Computational Physics 136*(1), 214 – 226.

[16] Remaitre, A.and van Asch, T. J., J. P. Malet, and O. Maquaire (2008). Influence of check dams on debris-flow run-out intensity. *Natural Hazards and Earth System Sciences* (8), 1403–1416.

[17] Silva, M., S. Costa, and A. H. Cardoso (2015). Slit check-dams for stony type debris flows mitigation. experimental study to evaluate sediment control efficiency. In *Second International Dam World Conference*.

[18] Vetsch, D. (2011). *Numerical Simulation of Sediment Transport with Meshfree Methods*. Ph. D. thesis, ETH Zurich.

[19] Zeng, Q. L., Z. Q. Yue, Z. F. Yang, and X. J. Zhang (2008). A case study of long term field performance of check-dams in mitigation of soil erosion in jiangjia stream, china. *Environmental Geology* (58), 897–911.